

# Prospects for ultra-high-energy particle acceleration at relativistic shocks

Zhi-Qiu Huang,<sup>1</sup> Brian Reville,<sup>1</sup> John G. Kirk,<sup>1</sup> Gwenael Giacinti,<sup>2,3,1</sup>

<sup>1</sup>Max-Planck-Institut für Kernphysik, Postfach 10 39 80, 69029 Heidelberg, Germany

<sup>2</sup>Tsung-Dao Lee Institute, Shanghai Jiao Tong University, Shanghai 201210, P. R. China

<sup>3</sup>School of Physics and Astronomy, Shanghai Jiao Tong University, Shanghai 200240, P. R. China

15 May 2023

## ABSTRACT

We study the acceleration of charged particles by ultra-relativistic shocks using test-particle Monte-Carlo simulations. Two field configurations are considered: (i) shocks with uniform upstream magnetic field in the plane of the shock, and (ii) shocks in which the upstream magnetic field has a cylindrical geometry. Particles are assumed to diffuse in angle due to frequent non-resonant scattering on small-scale fields. The steady-state distribution of particles' Lorentz factors is shown to approximately satisfy  $dN/d\gamma \propto \gamma^{-2.2}$  provided the particle motion is scattering dominated on at least one side of the shock. For scattering dominated transport, the acceleration rate scales as  $t_{\text{acc}} \propto t^{1/2}$ , though recovers Bohm scaling  $t_{\text{acc}} \propto t$  if particles become magnetised on one side of the shock. For uniform field configurations, a limiting energy is reached when particles are magnetised on both sides of the shock. For the cylindrical field configuration, this limit does not apply, and particles of one sign of charge will experience a curvature drift that redirects particles upstream. For the non-resonant scattering model considered, these particles preferentially escape only when they reach the confinement limit determined by the finite system size, and the distribution approaches the escapeless limit  $dN/d\gamma \propto \gamma^{-1}$ . The cylindrical field configuration resembles that expected for jets launched by the Blandford & Znajek mechanism, the luminous jets of AGN and GRBs thus provide favourable sites for the production of ultra-high energy cosmic rays.

**Key words:** acceleration of particles — shock waves — cosmic rays

## 1 INTRODUCTION

Relativistic shocks occur in many astrophysical sources of non-thermal emission such as pulsars, gamma-ray bursts (GRBs), micro-quasars and active galactic nuclei (AGN) and there is a growing wealth of observational evidence indicating that these shocks efficiently convert a large fraction of the energy they process into extremely energetic particles. Acceleration by the first-order Fermi mechanism operating at shocks has been proposed and thoroughly investigated by numerical and analytical approaches for the case of parallel shocks. However, interpreting recent observations, in particular those at very high energy (MAGIC Collaboration et al. 2019; Abdalla et al. 2019; H. E. S. S. Collaboration et al. 2021), requires a clear understanding of, at the very least, the spectral index predicted and the maximum particle energy achievable under more realistic physical conditions. Even in the test-particle approximation, our knowledge of these quantities remains incomplete.

Our goal in this work is to use test-particle Monte Carlo simulations to predict these quantities in two relevant field configurations: that of a uniform magnetic field, and that of a cylindrically symmetric field around a current carrying axis, such as can be expected in the jets that are either directly observed or inferred in all of the classes of object listed above. In each case we concentrate on a planar, perpendicular shock front — one in which the magnetic field and the shock lie in the same plane. This is the generic situation downstream of a highly relativistic shock front, since the component of the field in the shock plane is compressed by roughly the Lorentz factor of the

shock, whereas the component along the shock normal is unchanged (Begelman & Kirk 1990).

The test-particle theory of particle acceleration at relativistic shocks was mostly developed in the decade following the original works outlining the non-relativistic theory (see, for example, Kirk & Duffy 1999, for a review.) Two complementary approaches have been used: (i) Monte-Carlo simulation in which particles move in a simple, prescribed magnetic field geometry whilst undergoing stochastic transport, either represented as a sequence of small-angle scattering events (e. g. Kirk & Schneider 1988; Ostrowski 1993; Summerlin & Baring 2012) or, more formally, treated using stochastic differential equations (Achterberg et al. 2001; Takamoto & Kirk 2015) and (ii) direct numerical integration of particle orbits in a synthetically constructed, turbulent magnetic field (e. g. Ballard & Heavens 1991; Niemiec et al. 2006; Lemoine & Revenu 2006). Both methods have the drawback that they rely on a poorly constrained prescription for the turbulence. However, the former method, which we adopt here, has the advantages that it can be benchmarked against approximate analytic solutions, can model the energy dependent scattering expected to arise from self-excited fluctuations, and requires relatively modest computing resources.

Kinetic particle-in-cell (PIC) simulations do not have the fundamental limitations inherent in the test-particle approximation and have recently advanced towards a self-consistent study of relativistic shocks (Vanthieghem et al. 2020; Sironi et al. 2021; Bresci et al. 2023). In such simulations, Fermi acceleration is routinely observed

as a consequence of shock formation, at least for those shocks in which the upstream medium is sufficiently weakly magnetized. These simulations provide valuable insights into the physical processes that initiate acceleration, and, although they are currently limited to a narrow range of energy and length scales, nevertheless motivate the form of the scattering operator used in our analytical and Monte-Carlo work.

In the light of GRB afterglow detections at TeV gamma-ray energies, [Huang et al. \(2022a\)](#) used these insights to place constraints on the maximum electron energy expected at an ultra-relativistic shock. This revealed tension between observations and the simple one-zone synchrotron self-Compton emission model. A partial resolution was proposed in a companion paper ([Kirk et al. 2023](#)), which used both analytical and Monte-Carlo methods to show that a strong, uniform downstream magnetic field does not necessarily inhibit acceleration, as had previously been supposed ([Achterberg et al. 2001](#)). Here, we extend these studies in section 3.1, using the Monte-Carlo method to quantify the maximum energy reached at a shock front in a uniform magnetic field scenario.

While the uniform field configuration is instructive and can be applied in many cases, it is inadequate when the length scales associated with the highest energy particles become comparable to those of preexisting structure in the magnetic field. One interesting example is that of the termination shock of a pulsar wind, since particles accelerated at latitudes within one gyroradius of the equatorial current sheet can experience a reversal of the magnetic field during their excursions both upstream and downstream. This situation was treated using the synthetic field method by [Giacinti & Kirk \(2018\)](#) and global PIC simulations were performed by [Cerutti & Giacinti \(2020\)](#). In each case, spectra harder than those predicted for relativistic shocks in a homogeneous magnetic field were observed (see also [Cerutti et al. 2013](#); [Contopoulos & Stefanou 2019](#)).

Motivated by this finding, and by the fact that jets are a common feature in the sources of interest, we consider, in section 3.2, the related configuration of a cylindrically symmetric magnetic field. This is a reasonable model of the field upstream of the termination shock of a current-carrying jet, or upstream of the forward shock of an explosion that propagates along the rotation axis of a progenitor star into its magnetized wind. We identify a spectral break from the standard result at lower energy to one with a harder index at higher energy. As in the case addressed by [Giacinti & Kirk \(2018\)](#), the new component consists of particles of only one sign of charge. We find that the harder spectral index is almost independent of the level of scattering and that this component can extend to extremely high energy, limited only by the transverse size of the jet.

The paper is organized as follows. In Section 2, we motivate the transport model that we implement in our Monte-Carlo method. Numerical results for the uniform and cylindrical field cases are presented in Sections 3.1 and 3.2, respectively, and the implications and limitations of our results are discussed in Section 4.

## 2 TEST-PARTICLE TRANSPORT

The distribution function  $f(t, \mathbf{x}, \mathbf{p})$  in phase space  $(\mathbf{x}, \mathbf{p})$  of test particles that undergo small-angle, elastic scatterings satisfies the Fokker-Planck equation

$$\frac{\partial f}{\partial t} + \dot{\mathbf{x}} \cdot \frac{\partial f}{\partial \mathbf{x}} + \dot{\mathbf{p}} \cdot \frac{\partial f}{\partial \mathbf{p}} = \frac{\nu_{\pm}}{2} \Delta_{\mathbf{p}} f, \quad (1)$$

where  $\Delta_{\mathbf{p}}$  is the angular part of the Laplacian in momentum space,  $\nu_{\pm}$  the isotropic scattering rate (that can depend on  $\mathbf{x}$  and  $\mathbf{p}$ ) and

$(\dot{\mathbf{x}}, \dot{\mathbf{p}})$  are the time derivatives of an unscattered trajectory in phase space. Equation (1) applies in a reference frame, called the local fluid frame, in which the electric field vanishes. The unscattered trajectories of a particle of charge  $q$  and mass  $m$  are then determined by the large-scale, static magnetic field  $\mathbf{B}$ , i. e.,  $\dot{\mathbf{p}} = q(\dot{\mathbf{x}} \times \mathbf{B})/c$ . In the presence of a shock front that lies in the plane  $x = 0$  in cartesian coordinates, the two fluid frames of interest are the upstream  $x > 0$ , suffix “+” and downstream  $x < 0$ , suffix “−”, frames, each with a corresponding scattering rate  $\nu_{\pm}$ . We will assume, for simplicity, that these frames are connected by a Lorentz boost in the  $x$ -direction. Length and timescales in the local frame are conveniently normalized using the non-relativistic gyrofrequency  $\omega_{\pm} = |qB_{0\pm}|/mc$  associated with an upstream/downstream fiducial field strength  $B_{0\pm}$ . When a trajectory reaches the shock front, it is assumed to emerge into the region on the other side without changing its momentum.

The nature of the particle transport and, hence, the spectrum and angular distribution of accelerated particles, depends on the relative importance of scattering and deflection in the large-scale field in each half-space. For sufficiently weakly magnetized shocks, the Weibel instability, which operates initially on the scale of the plasma skin-depth, drives the growth of highly non-linear magnetic field structures in the shock-transition region, extending both into the upstream and downstream regions (e. g. [Sironi et al. 2013](#); [Vanthieghem et al. 2020](#)). Assuming these structures remain small compared to the gyroradius of a test particle, they are responsible for nonresonant scattering. Then, following [Kirk & Reville \(2010\)](#), for a characteristic fluctuation length scale  $\lambda$  of volume averaged root mean square amplitude  $\delta B$ , the mean scattering angle per fluctuation is  $\Delta\theta \approx |q|\delta B\lambda/pc$ . Taking the mean time between scatterings to be  $\lambda/c$  one finds a scattering rate proportional to  $p^{-2}$ , characteristic of non-resonant interactions:

$$\nu_{\pm} = \nu_{0\pm} (p/mc)^{-2}, \quad (2)$$

where

$$\nu_{0\pm} = (\delta B/B_{0\pm})^2 \omega_{\pm}^2 \lambda/c \quad (3)$$

is independent of particle energy.

Simulations are required to determine the properties of  $\delta B$  and  $\lambda$ . Filamentary structures driven by the Weibel instability typically develop on length-scales  $\lambda = 10 - 100c/\omega_{\text{pi}}$  where  $\omega_{\text{pi}} = \sqrt{4\pi n^2 e^2 c^2/w}$  is the relativistically corrected plasma frequency, with  $w$  the enthalpy density. The growth of longer wavelength fluctuations in the foreshock region was investigated for unmagnetized ([Medvedev & Zakutnyaya 2009](#)) and magnetized ([Reville & Bell 2014](#)) ambient plasma conditions (see also [Milosavljević & Nakar 2006](#)). However, a complete multi-scale theory of turbulent field generation at ultra-relativistic shocks does not exist at present, and for simplicity, we therefore treat the scattering rate as a free parameter that can take different values upstream or downstream, but is otherwise homogeneous.

We employ a Monte-Carlo code — see Appendix A — to construct time-dependent solutions of Eq. (1) upstream and downstream of a relativistic shock front, measuring  $f$  at the shock front and assuming an injection term that is zero for  $t < 0$  and constant for  $t > 0$ .

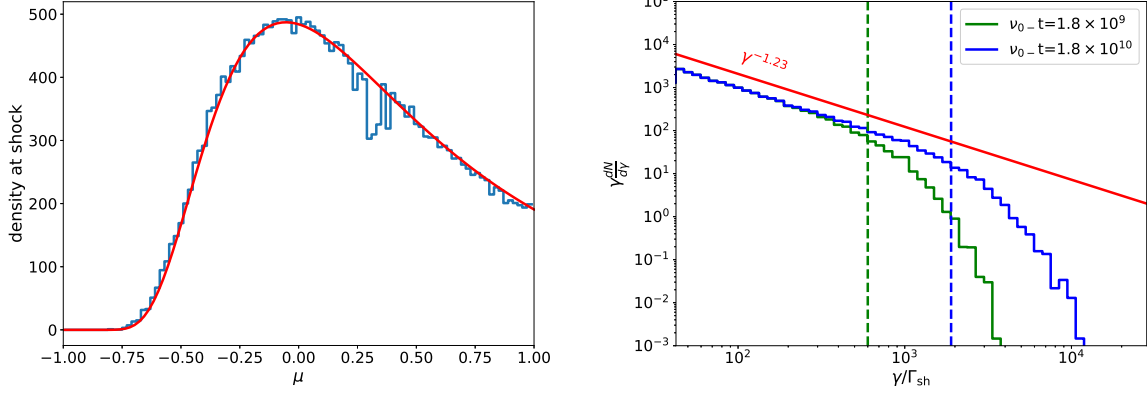


**Figure 1.** Results for the case of negligible large-scale magnetic field (equivalent to the parallel shock case), shown in the downstream frame. Left panel: The dependence of the phase space density  $f$  at the shock front on the cosine  $\mu$  of the angle between  $\mathbf{p}$  and the shock normal (blue) compared to the analytic approximation. Right panel: the dependence of  $\gamma dN/d\gamma = \gamma^3 f$  at the shock front on the normalized particle Lorentz factor  $\gamma/\Gamma_{\text{sh}}$  at two different times, compared to the predicted power-law (red line) and the estimated maximum energy at the chosen times (green and blue vertical lines, see eq (5))

### 3 RESULTS

#### 3.1 Uniform magnetic field

##### 3.1.1 Parallel shock

We first use our code to revisit the case in which the large-scale field can be neglected. This is equivalent to the case of an exactly parallel shock front, in which the strength of the magnetic field plays no role. We adopt a constant Lorentz factor  $\Gamma_{\text{sh}} = 50\sqrt{2}$  for the shock, as seen by an upstream observer, and a downstream shock speed of  $\beta_d = 1/3$ , as expected from the hydrodynamic jump conditions for an ultra-relativistic shock propagating in a cold gas. This case is not expected to differ significantly from the ultrarelativistic limit (Kirk et al. 2023), where an analytic approximation is known for the stationary (time-asymptotic) distribution function at  $\gamma \gg \Gamma_{\text{sh}}$  and estimates of the acceleration rate are available, thereby enabling the code to be benchmarked.

Fig. 1 shows the angular distribution of particles at the shock front (left) and the accelerated particle spectrum (right), both measured in the downstream frame. (In the angular distribution, we record only those particles with energy larger than 30 times that of injection, for which no memory of the injection conditions remains. In the spectrum we plot the number of these particles per logarithmic energy interval,  $\gamma dN/d\gamma = \gamma^3 f$ .) For comparison, we plot, in the left panel, the angular dependence of the leading eigenfunction (Kirk et al. 2000), which shows close agreement with our simulation results. We note the feature associated with particles that graze the shock, here occurring at  $\mu = 1/3$ .

In the right panel, we compare the expected time-asymptotic power law spectrum with the simulation results at two different times. Below a cut-off,  $\gamma_c(t)$ , that advances to higher energy with increasing time, the distribution is found to match closely the predicted stationary value  $\gamma dN/d\gamma \propto \gamma^{-1.23}$  ( $f \propto \gamma^{-4.23}$ ) for an ultrarelativistic shock. The time-dependent position of this cut-off, is predicted by equating the energy dependent acceleration timescale with the time elapsed since injection started (see eq (43) in Achterberg et al. 2001). The acceleration timescale is simply the sum of the average time spent upstream,  $\Delta t_+$ , and downstream,  $\Delta t_-$  — both measured in the downstream rest frame — during one cycle (which starts at

the shock, crosses it once and then returns to it). When scattering dominates both up and downstream,

$$\begin{aligned} \Delta t_+ &= \gamma^2 / (\Gamma_{\text{sh}} v_{0+}) \\ \Delta t_- &= \gamma^2 / v_{0-}, \end{aligned} \quad (4)$$

therefore,

$$\gamma_c(t) = t^{1/2} \left( \frac{1}{v_{0-}} + \frac{1}{\Gamma_{\text{sh}} v_{0+}} \right)^{-1/2}. \quad (5)$$

In Fig 1 we adopt  $v_{0+} = v_{0-}$ , in which case accelerating particles spend most of their time in the downstream region during one complete cycle. Since the shock does not decelerate and losses and boundary effects are neglected, the cut-off increases indefinitely. However, its rate of increase slows down because of the quadratic dependence of the scattering time on energy (cf. Stockem et al. 2012; Sironi et al. 2013; Plotnikov et al. 2018). The time-dependent spectrum softens significantly above the Lorentz factor given by Eq. (5), shown in the figure as green and blue vertical lines.

##### 3.1.2 Perpendicular shock

We next consider the case where the regular magnetic field is perpendicular to the shock normal. This *perpendicular* shock is the generic configuration for relativistic shocks, because the velocity of the point of intersection of a magnetic field line and the shock surface exceeds  $c$  unless the shock normal happens to be aligned with the upstream magnetic field to within an angle of  $1/\Gamma_{\text{sh}}$ . (Note that all such *superluminal shocks* can be transformed into perpendicular shocks by a Lorentz boost along the shock surface.) The downstream magnetic field is determined by the ideal magneto-hydrodynamic shock jump conditions for a weakly magnetized ultra-relativistic shock i. e.,  $B_- = 2\sqrt{2}\Gamma_{\text{sh}}B_+$  (e. g. Kirk & Duffy 1999), where  $B_{\pm}$  are measured in the corresponding rest frame of the plasma. Since the fields up and downstream are uniform, they can be taken to equal their fiducial values  $B_{\pm} \equiv B_{0\pm}$ . We again adopt  $\Gamma_{\text{sh}} = 50\sqrt{2}$  and set  $v_{0-} = 3 \times 10^4 \omega_-$ .

The guiding centre of a magnetized particle downstream of a superluminal, relativistic shock recedes from the shock front at a sub-

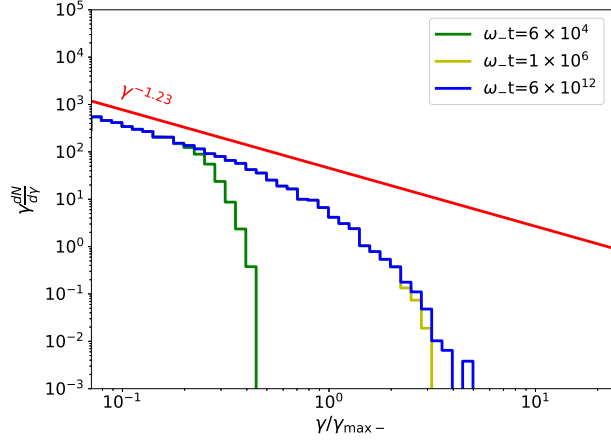


**Figure 2.** The particle spectra at a perpendicular shock in a uniform magnetic field with relatively weak scattering upstream  $v_{0+} = 10^{-4}v_{0-}$ , as a function of the ratio of the Lorentz factor to its predicted maximum,  $\gamma_{\max-} = v_{0-}/\omega_- = 3 \times 10^4$ , see eq (6). The upstream magnetized limit,  $\gamma_{\max+} \approx 600$ , lies close to the injection energy and is not shown.

stantial fraction of  $c$ , which led [Achterberg et al. \(2001\)](#) to the assertion that Fermi acceleration would be ineffective in the absence of strong cross-field transport (i. e., strong scattering) downstream. As a consequence, they presented results only for  $\omega_- = 0$ . The two limiting cases of strong and weak scattering upstream ( $\omega_+ = 0$  and  $v_+ = 0$ , respectively) were investigated and yielded results which did not differ significantly from the analytic approximation for the parallel shock case ( $\omega_+ = \omega_- = 0$ ) treated in section 3.1.1.

Since we take account of the energy dependence of  $v_{\pm}$ , these different scattering regimes map into different ranges of Lorentz factors for the accelerated particles. Thus, strong and weak scattering downstream correspond to  $\gamma \ll \gamma_{\max-}$  and  $\gamma \gg \gamma_{\max-}$ , respectively, where

$$\gamma_{\max-} = v_{0-}/\omega_- \quad (6)$$

is the *downstream magnetized limit* to which we refer in [Huang et al. \(2022a\)](#). Similarly, it is possible to define a corresponding upstream limit, taking account of the fact that a particle is scattered or deflected through only a small angle  $\sim 1/\Gamma_{\text{sh}}$  whilst upstream, before being overtaken by the shock:

$$\gamma_{\max+} = 2\sqrt{2}\Gamma_{\text{sh}}v_{0+}/\omega_- \quad (7)$$

Simulations are shown in Fig 2, for  $v_{0+} = 10^{-4}v_{0-}$ , implying  $\gamma_{\max-} = 3 \times 10^4$  and  $\gamma_{\max+} \approx 600 \ll \gamma_{\max-}$ . The stationary, power-law part of the spectrum remains close to the analytic prediction, whereas the time-dependent cut off advances well beyond  $\gamma_{\max+}$ . In this case, particles in the range  $\gamma_{\max+} \ll \gamma \ll \gamma_{\max-}$  suffer deflection rather than scattering whilst upstream and the average time they spend there is

$$\begin{aligned} \Delta t_+ &= 2\sqrt{2}\gamma/\omega_- \\ &\approx (3\gamma_{\max-}/\gamma)\Delta t_- \end{aligned} \quad (8)$$

Thus, they spend most of a cycle in the upstream, and the cut-off advances with time in this range according to  $\gamma_c(t) \approx \omega_-t/3$ , i. e., essentially at the rate corresponding to *Bohm* scattering (see section 4). Nevertheless, close to  $\gamma_{\max-}$ , eq (5) remains a good order of magnitude estimate, since here particles divide their time almost equally between the two regions. At  $\omega_-t = 6 \times 10^4$ ,  $\gamma_c(t)$  is roughly a factor of

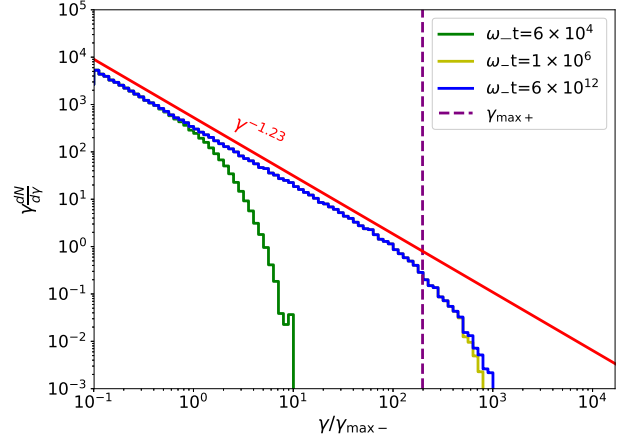


**Figure 3.** Particle spectra at a perpendicular shock in a uniform magnetic field, with relatively strong scattering upstream:  $v_{0+} = v_{0-}$  and  $v_{0-}/\omega_- = 3 \times 10^4 = \gamma_{\max-}$ , plotted as a function of  $\gamma/\gamma_{\max-}$ . The vertical dashed line shows the upstream magnetized limit,  $\gamma_{\max+}$ , see eq (7).

3 less than  $\gamma_{\max-}$ , whereas at  $\omega_-t > 10^6$  a stationary state is reached at essentially all energies to which particles can be accelerated, confirming that saturation occurs at roughly  $\gamma_{\max-}$ , in agreement with the findings of [Achterberg et al. \(2001\)](#).

If, however,  $\gamma_{\max+} \gg \gamma_{\max-}$ , the situation changes. In Fig. 3 we show results for  $v_{0+} = v_{0-}$ , implying  $\gamma_{\max-} = 3 \times 10^4$  and  $\gamma_{\max+} = 6 \times 10^6 \gg \gamma_{\max-}$ . In this case the power-law spectrum does not cut off at the downstream magnetized limit, but extends up to  $\gamma_{\max+}$ . Particles in the range  $\gamma_{\max-} \ll \gamma \ll \gamma_{\max+}$  now spend most of a cycle in the downstream region, from which they are ejected after a fraction of a gyration:

$$\begin{aligned} \Delta t_- &= \gamma/\omega_- \\ &\approx (\gamma_{\max+}/3\gamma)\Delta t_+ \end{aligned} \quad (9)$$

Once again, therefore, the cut-off advances linearly with time:  $\gamma_c(t) \approx \omega_-t$ , corresponding to *Bohm* scattering.

The stationary spectra in the regime  $\gamma_{\max-} \ll \gamma \ll \gamma_{\max+}$  were analyzed by [Kirk et al. \(2023\)](#), using both our Monte-Carlo code and an analytic approximation scheme. For  $\Gamma_{\text{sh}} > 50$  a power-law spectrum with index  $f \propto \gamma^{-4.17}$  was found. However, the transition from a power-law of index 1.23 to one of 1.17 is not discernible in Fig 3, because of the relatively small range of Lorentz factors between  $\gamma_{\max-}$  and  $\gamma_{\max+}$ .

We note that in the case of an oblique shock front, it is only the component of the magnetic field perpendicular to the shock normal in the upstream that causes particles to leave the narrow cone in which they can move ahead of the shock front. This implies that the *upstream* magnetized limit may depend on the shock obliquity for superluminal shocks, even though the regular magnetic field in the downstream remains almost perpendicular to the shock normal. Denoting by  $\alpha$  the angle between the upstream magnetic field, as measured by an upstream observer, and the shock normal, we find

$$\gamma_{\max+} = 2\sqrt{2}\Gamma_{\text{sh}}v_{0+}/(|\sin\alpha|\omega_-), \text{ for } |\sin\alpha| > 1/\Gamma_{\text{sh}}, \quad (10)$$

generalizing eq (7). We have performed additional simulations that confirm this increase.



### 3.2 Magnetic field with cylindrical symmetry

To model the situation of either a reverse shock in a magnetized jet, or the forward shock of a jet that propagates along the rotation axis into a medium whose magnetic structure mimics the *Parker wind*, we choose a simple geometry for the static magnetic field in the upstream region: one in which only azimuthal field components exist in cylindrical coordinates  $(\rho, \theta, x)$ . Satisfying the solenoidal field condition then requires that  $\partial B_\theta / \partial \theta = 0$ . To maintain a finite current in the jet, the field should approach zero on the symmetry axis. Therefore, we select a large-scale upstream field  $\mathbf{B}_+$  that increases linearly with cylindrical radius  $\rho$  out to a distance  $\rho_0$ , outside of which it remains constant. As in the homogeneous case, we assume that it is compressed upon crossing the shock front, which remains in the plane  $x = 0$  and is, therefore, also a perpendicular shock:

$$\mathbf{B}_\pm = B_{0\pm} \hat{\boldsymbol{\theta}} \times \begin{cases} (\rho/\rho_0), & \rho \leq \rho_0 \\ 1, & \rho_0 < \rho \leq \rho_{\max}. \end{cases} \quad (11)$$

This field corresponds to a constant axial current density within  $\rho_0$ , outside of which it falls off as  $1/\rho$ . We set a boundary at  $\rho = \rho_{\max} \gg \rho_0$ , and assume that all particles that reach it escape. In this way,  $\rho_0$  models the thickness of the current carrying region around the axis, which is likely to be determined by microphysical processes, whereas  $\rho_{\max}$  models the macroscopic geometry of the field, comparable, for example, to the distance of the shock from the central object/engine. Since times and distances are normalized to the nonrelativistic gyro frequency and radius corresponding to  $B_{0-}$ , particles with  $\gamma \gg \rho_0$  cross the axial region without significant deflection by the magnetic field, and particles with  $\gamma > \rho_{\max}$  cannot be confined within the system, when downstream. When these particles enter the upstream region, their gyro radius increases by a factor  $\sim \Gamma_{\text{sh}}^2$ . However, the constraints on sensitivity to the axial region and on confinement are unchanged, because their angular distribution is tightly beamed along the axis.

In the simulations presented here we set  $\rho_0 = 10^5$  and  $\rho_{\max} = 10^7$ . As in section 3.1, we select  $\Gamma_{\text{sh}} = 50\sqrt{2}$  and  $v_{0-} = 3 \times 10^4 \omega_-$ , but note that  $\omega_-$  is defined by the fiducial field  $B_{0-}$ , so that scattering is always dominant sufficiently close to the axis  $\rho = 0$ . Particles are initially injected at  $\rho = 0$ , with an isotropic angular distribution immediately downstream of the shock front.

The corresponding spectra for weak upstream scattering,  $v_{0+} = 10^{-4} v_{0-}$ , are shown in Fig. 4. The results shown in yellow are for test particles with the same sign of charge as the fiducial field,  $qB_{0-} > 0$ , whereas those in blue are for  $qB_{0-} < 0$ . These two spectra are essentially identical at low energy, but diverge above a Lorentz factor given roughly by the downstream magnetized limit  $\gamma_{\max-}$ . In the downstream region, the transport of particles of lower Lorentz factor is everywhere dominated by scattering, so that spectrum remains close to that expected in the parallel shock case, or, equivalently, in the perpendicular shock with  $\gamma_{\max+} \ll \gamma_{\max-}$  (Fig 2).

At Lorentz factors greater than  $\gamma_{\max-}$ , however, there is a dramatic difference: the blue spectrum cuts off, whereas the yellow spectrum hardens to higher energy until the confinement limit  $\gamma \approx \rho_{\max}$  is reached.

In a uniform field, the only drift present is the  $\mathbf{E} \times \mathbf{B}$  drift, that causes particles to be dragged along at the speed of the local plasma flow, independent of their charge. In the cylindrically symmetric field, however, a charge-dependent curvature drift is superposed on the  $\mathbf{E} \times \mathbf{B}$ -drift. For  $qB_0 > 0$ , this drift is directed in the positive  $x$  direction, i. e., in the direction of propagation of the shock front. The drift speed is slow far from the axis but is  $\sim c$  when  $\rho < \gamma$ . As a con-

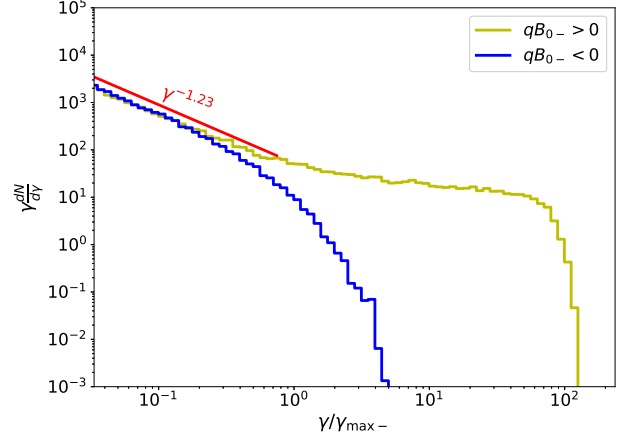


**Figure 4.** Particle spectra in a cylindrically symmetric magnetic field. Here we consider weak scattering in the upstream,  $v_{0+} = 10^{-4} v_{0-}$ . The yellow and blue histograms show results for  $qB_{0-} > 0$  and  $qB_{0-} < 0$ , respectively, plotted as functions of  $\gamma/\gamma_{\max-}$  ( $\gamma_{\max-} = 3 \times 10^4$ ). The simulations were run until a steady state was reached. For  $qB_{0-} > 0$  a cut off appears at roughly the confinement limit,  $\gamma \approx \rho_{\max} = 10^7$ .

sequence, particles with  $qB_{0-} > 0$  that are located close to the axis in the downstream region and experience little scattering, are able to catch up and overtake the shock, whereas those with  $qB_{0-} < 0$  are swept away from it. This behaviour is illustrated in the lower panels of fig. 5, where we show a trajectory typical of a particle with  $qB_{0-} > 0$  and a Lorentz factor  $> \gamma_{\max-}$ .

The situation is reversed in the upstream region, where particles with  $qB_{0-} > 0$  tend to outrun the shock front — see the upper panel of fig. 5. However, even a very low scattering rate there suffices eventually to deflect particles through an angle that allows them to be caught again by the shock front. Therefore, these particles can be accelerated beyond the limit  $\gamma_{\max+}$  given in eq (7), provided the upstream region is sufficiently extended in the  $x$ -direction. This can be seen in Fig. 6, where we run the simulation without imposing a boundary on the radial extent of the magnetic field. In the presence of scattering, particles can then escape only by being swept far downstream. In this case, as in the case of a parallel shock in a uniform field, there is no intrinsic upper limit on the energy to which favourably charged particles located close to the axis can be accelerated, and the spectrum below the time-dependent upper cut-off approaches  $f \propto \gamma^{-3}$ , as expected for particles that are effectively confined to the vicinity of the shock front. Because the acceleration rate is now limited by the time spent upstream, the cut off advances according to  $\gamma_c(t) \approx \sqrt{\Gamma_{\text{sh}} v_{0+} t}$ .

Particles far from the axis do not benefit from the curvature drift. Hence, the positions at which particles are injected affects the accelerated spectrum. We demonstrate this effect in fig 7, where particles are injected at positions that are uniformly distributed in  $\rho$  between the axis and  $\rho_{\max}$ . Many of these particles remain far away from the axis and populate a spectrum with index  $f \propto \gamma^{-4.23}$  and a cut off close to  $\gamma_{\max-}$ . Only a small fraction of them reaches this energy whilst sufficiently close to the axis — i. e., at  $\rho < \gamma_{\max-}$  — to achieve a substantial drift velocity. These are then accelerated further into a hard spectrum that extends up to the confinement limit. In Fig. 7,  $\rho_{\max}$  is reduced by a factor of 2 relative to that used in Fig. 4, and the maximum energy decreases by the same factor, thereby vali-

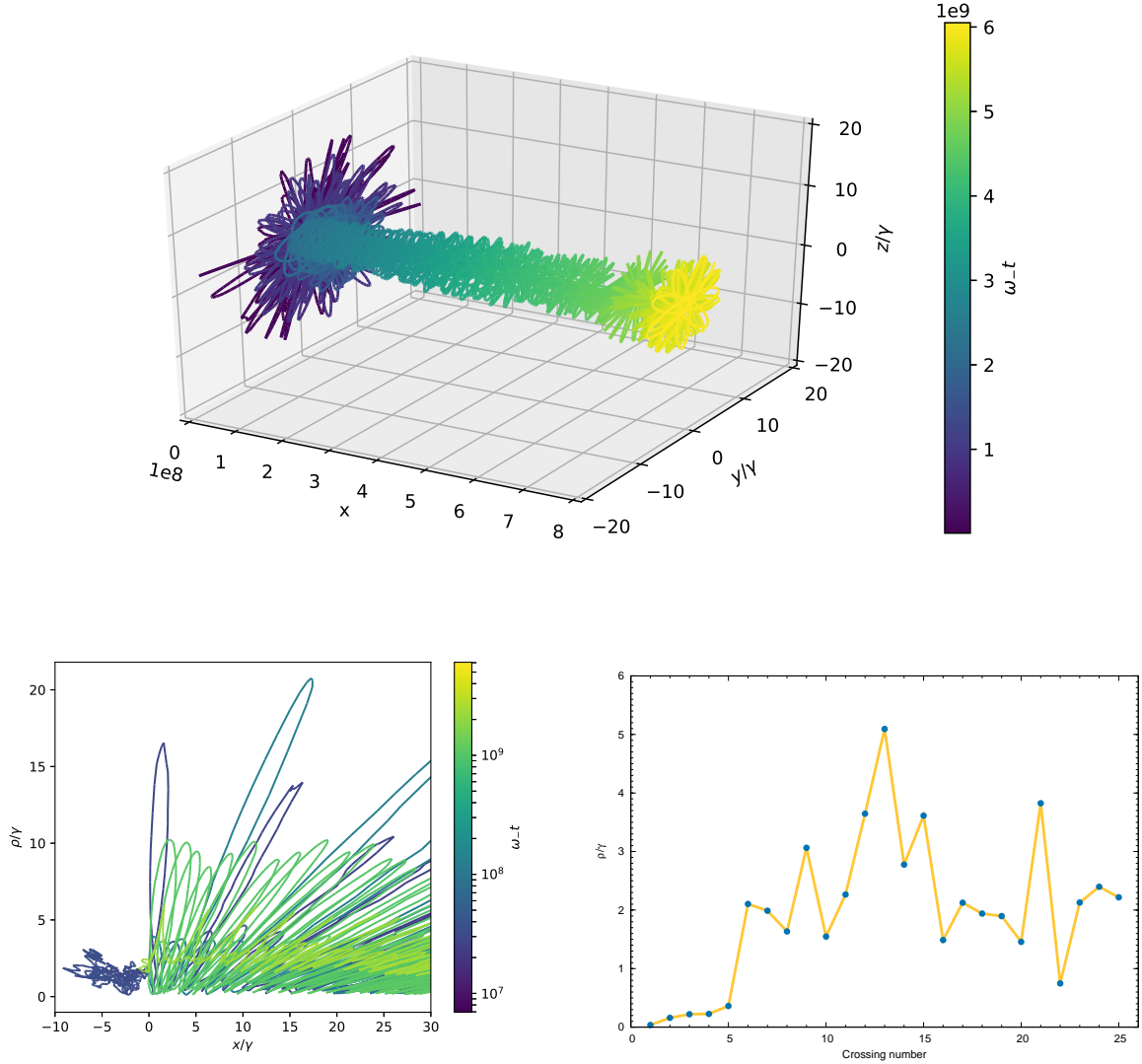


**Figure 5.** Trajectory in the shock rest frame of a particle with  $qB_{0-} > 0$  and Lorentz factor above  $\gamma_{\max-}$ . Top panel: Particle trajectory in 3-dimensional space before escaping from the boundary  $\rho_{\max}$  in the upstream region. Bottom left panel: the trajectory in the  $x$ - $\rho$ -plane near the shock front, showing a total of 25 crossings. Bottom right panel: The value of  $\rho/\gamma$  each time the trajectory crosses the shock front, showing that the trajectory is confined to a region close to the axis where the drift speed is  $\sim c$ .

dating our assertion that particles are accelerated to the confinement limit.

#### 4 DISCUSSION

The main results of this paper concern the energy spectrum of highly energetic charged particles that can be produced by a relativistic shock front. They fall into two parts, each of which addresses an idealized situation.

In the first, we consider a planar shock front that propagates into a medium containing a relatively weak, perfectly uniform magnetic field, upon which fluctuations are imposed. We assume that the uniform field lies in the plane of the shock front, i. e., the shock is *perpendicular*, since this is by far the most likely configuration for a relativistic shock front. The spectrum produced then depends on the strength and length scale of the fluctuations. Assuming these are

of short length scale, as suggested by PIC simulations, we find that there is an intrinsic limit on the energy to which particles can be accelerated, even when other effects, such as radiative losses, or the finite size or finite lifetime of the system, can be neglected. This is in marked contrast to the (presumably less realistic) situation at a parallel shock front, which does not possess such an intrinsic limit. On the other hand, we find that the time-asymptotic particle spectrum below this limiting energy is essentially the same as that predicted for a parallel shock, and does not depend on the strength of the fluctuations.

The limit itself, however, does depend on the strength of the fluctuations in both the upstream and downstream plasma. If these are more effective in the downstream than the upstream, we confirm the maximum energy predicted by [Huang et al. \(2022a\)](#) (the “magnetized limit”), denoted here as  $\gamma_{\max-}$  in eq (6). In the converse situation, we confirm the spectral index indeed remains close to that of a parallel shock, as predicted by [Kirk et al. \(2023\)](#), and find a

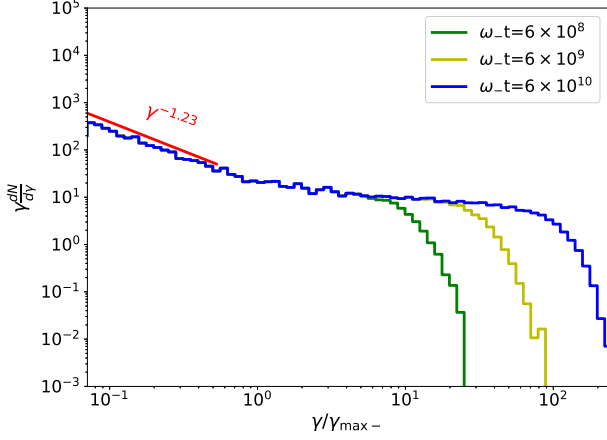


**Figure 6.** Spectra for particles with  $qB_{0-} > 0$  and the same parameters as in fig 4, but without an upper limit on  $\rho$ . The cutoff on the hard component of the spectrum does not saturate, but increases monotonically with time according to  $\gamma_c(t) \propto t^{1/2}$ .

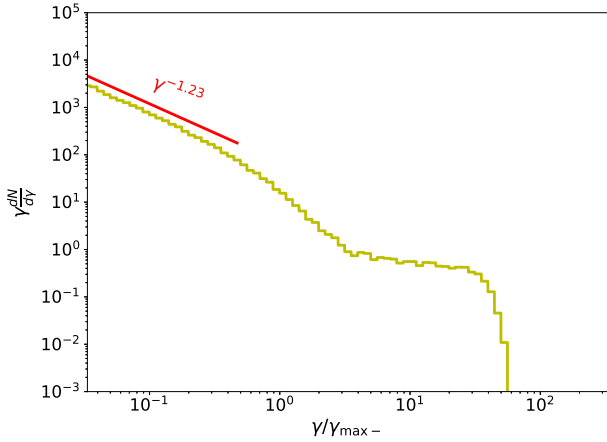


**Figure 7.** The spectrum for particles with  $qB_{0-} > 0$  and the same parameters as in fig 4, but with an upper limit on the jet radius reduced by a factor of 2, i. e.,  $\rho_{\max} = 5 \times 10^6$ . Also, particles are now injected with a uniform distribution in  $\rho$  between the axis  $\rho = 0$  and  $\rho_{\max}$ . Only those that reach  $\gamma \approx \gamma_{\max-}$  when close to the axis are accelerated further.

new expression for the upper limit,  $\gamma_{\max+}$ , given in eq (7). In each case, we find that the spectrum evolves with an upper cut-off energy that increases linearly with time, as it approaches the limiting value, which is determined by the larger of the two quantities  $\gamma_{\max\pm}$ . This behaviour is the same as that predicted under the assumption of *Bohm* scattering, where the mean free path of a particle is assumed to equal its gyroradius. In contrast, a time-dependence  $\gamma_c(t) \propto t^{1/2}$  is expected when particle transport is dominated *everywhere* by non-resonant scattering (Kirk & Reville 2010).

The model described above is necessarily highly idealized. For example, the assumption of a perfectly uniform background field is reasonable only if there are no fluctuations on a length scale comparable to the gyroradius of the highest energy particles. This fails

if resonant interactions become important. But, more importantly it also places a strict lower limit  $R_{\text{up}}$  on the length scale of structures that may pre-exist in the upstream medium. Although it is tempting to associate the length scale  $R_{\text{up}}$  with the overall size  $R$  of the astrophysical system under consideration, there are several situations in which it is expected to be much smaller. For example, MHD models of pulsar wind nebulae and jets from accreting black holes (see Porth et al. 2017; Davis & Tchekhovskoy 2020, for reviews) show both narrow current sheets and axial current flows, where  $R_{\text{up}} \ll R$ .

The second idealized situation we address is the latter: a relativistic shock propagating along the axis of a plasma containing a cylindrically symmetric field. In this situation, we find that the acceleration of particles with Lorentz factor  $\gamma < \gamma_{\max-}$  proceeds in the same manner as in a uniform field, since their transport is dominated by scattering in the downstream region. At higher energy, however, there is a dramatic difference for those particles that are located within roughly one gyroradius of the axis downstream of the shock. There, unscattered trajectories undergo rapid curvature drifting, which enables charges of favourable sign to catch up with the shock, thereby reducing their probability of escaping the acceleration region. As a result, we find a hard  $f \propto \gamma^{-3}$  spectrum (see Fig 4) for the favoured particles, that can extend up to the confinement limit  $\gamma \approx |qB_{0-}|R/mc^2$ . This is reminiscent of the findings of Giacinti & Kirk (2018), who integrated particle orbits directly in synthetically constructed magnetic turbulence. They considered the equatorial region of a pulsar wind termination shock, which contains a plane current sheet rather than an axial current, and observed a turbulence-dependent hardening of the spectrum of one of the charged components, which they interpreted as due to *Speiser orbits* that cross the sheet. In our case, the sheet is essentially contracted into the axis of the cylinder, so that it is not possible for a particle orbit to cross it. Nevertheless, curvature drift takes over the role of the Speiser orbits and permits particles of one charge to decouple from the downstream fluid motion and recross into upstream.

In interpreting our results, it is important to remember the limitations not only of our assumed scattering model, but also of the test particle approximation. For example, the very hard spectrum we find will, if it extends to high energy, begin to exert a significant influence on the background plasma, which is not included. In principle, PIC simulations are capable of accounting for this and other physical effects, but they are currently challenged by the large range of spatial and temporal scales that separate the thermal particles from the most energetic. Thus, global PIC simulations of both the equatorial current sheet and the axial current case show tantalising hints of a hard spectral component (Cerutti & Giacinti 2020, 2023), but set the confinement limit of the simulation to a particle Lorentz factor  $\sim 10^3$ . Consequently, a distinct hard spectral component does not emerge and the maximum energy permitted in the simulation is well below that expected in astrophysical objects. Similarly, PIC simulations of acceleration in uniform fields report acceleration rates approximately proportional to  $t^{1/2}$  (Stockem et al. 2012; Sironi et al. 2013; Plotnikov et al. 2018), but did not extend to energies above the lower of the two limits  $\gamma_{\max\pm}$ , above which we predict an unchanged spectral index and an acceleration rate  $\propto t$ .

Our principal findings on the maximum energy and spectral features have many potential applications for astrophysical sources which host relativistic shocks. Amongst the best known examples are GRBs, Pulsar wind termination shocks, and AGN/Blazars. All these source classes are well established gamma-ray emitters (e.g. Albert et al. 2021; Lhaaso Collaboration et al. 2021; H. E. S. S. Collaboration et al. 2021; Huang et al. 2022b) and/or hard X-ray synchrotron sources (e.g. Costamante et al. 2018;

Thimmappa et al. 2022). We find that the steady-state spectrum in almost all cases where pitch-angle diffusion dominates on at least one side of the shock is almost indiscernible from the well-known result  $dN/d\gamma \propto \gamma^{-2.2}$ , originally derived for exactly parallel shocks. Although such spectra are typical of those inferred from GRB afterglow observations, harder spectra are not uncommon (see for example Ajello et al. 2018). Our results indicate that large scale field structures associated to the specific geometry of the source, can maintain the shock acceleration cycles through the drift motions induced by this geometry. This naturally leads to a maximum energy close to the confinement limit, in contrast with the findings of Bell et al. (2018), who considered only self-excited turbulence. It also suggests a hardening of the spectrum which may, in principle, be identified with a spectral break. The asymptotic ‘zero-escape’ limit presented here;  $dN/d\gamma \propto \gamma^{-1}$  is a result of our simplified assumptions, and we anticipate a range of spectral shapes will be revealed in future environment-specific studies, in particular if feedback from the axial current on the upstream medium is included. Nevertheless, there are several clear examples where such hard spectra are favoured. It has been demonstrated, for example, that a hard source spectrum for UHECR alleviates the need to invoke problematic negative source evolution (Taylor et al. 2015). If relativistic jets, either those of GRBs or high power AGN, are the primary source of UHECRs, particles must be accelerated close to the confinement limit for these sources (see discussion in Blandford 2000; Matthews et al. 2020). Since these particles sample the full width of the jet, they naturally probe its large-scale underlying magnetic structure. In this regard, the origin of the highest energy cosmic rays in our local universe is a natural consequence of the mechanism that efficiently extracts the power from the central engine (Blandford & Znajek 1977).

## 5 DATA AVAILABILITY STATEMENT

No new data were generated or analysed in support of this research.

## REFERENCES

- Abdalla H., et al., 2019, *Nature*, **575**, 464  
 Achterberg A., Gallant Y. A., Kirk J. G., Guthmann A. W., 2001, *MNRAS*, **328**, 393  
 Ajello M., et al., 2018, *ApJ*, **861**, 85  
 Albert A., et al., 2021, *ApJ*, **911**, 143  
 Ballard K. R., Heavens A. F., 1991, *MNRAS*, **251**, 438  
 Begelman M. C., Kirk J. G., 1990, *ApJ*, **353**, 66  
 Bell A. R., Araudo A. T., Matthews J. H., Blundell K. M., 2018, *MNRAS*, **473**, 2364  
 Blandford R. D., 2000, *Physica Scripta Volume T*, **85**, 191  
 Blandford R. D., Znajek R. L., 1977, *MNRAS*, **179**, 433  
 Bresci V., Lemoine M., Gremillet L., 2023, *arXiv e-prints*, p. [arXiv:2303.11394](https://arxiv.org/abs/2303.11394)  
 Cerutti B., Giacinti G., 2020, *A&A*, **642**, A123  
 Cerutti B., Giacinti G., 2023, *arXiv e-prints*, p. [arXiv:2303.12636](https://arxiv.org/abs/2303.12636)  
 Cerutti B., Werner G. R., Uzdensky D. A., Begelman M. C., 2013, *ApJ*, **770**, 147  
 Contopoulos I., Stefanou P., 2019, *MNRAS*, **487**, 952  
 Costamante L., Bonnoli G., Tavecchio F., Ghisellini G., Tagliaferri G., Khangulyan D., 2018, *MNRAS*, **477**, 4257  
 Davis S. W., Tchekhovskoy A., 2020, *ARA&A*, **58**, 407  
 Giacinti G., Kirk J. G., 2018, *ApJ*, **863**, 18  
 H. E. S. S. Collaboration et al., 2021, *Science*, **372**, 1081  
 Huang Z.-Q., Kirk J. G., Giacinti G., Reville B., 2022a, *ApJ*, **925**, 182

- Huang Y., Hu S., Chen S., Zha M., Liu C., Yao Z., Cao Z., Experiment T. L., 2022b, GRB Coordinates Network, **32677**, 1  
 Kirk J. G., Duffy P., 1999, *Journal of Physics G Nuclear Physics*, **25**, R163  
 Kirk J. G., Reville B., 2010, *ApJ*, **710**, L16  
 Kirk J. G., Schneider P., 1988, *A&A*, **201**, 177  
 Kirk J. G., Guthmann A. W., Gallant Y. A., Achterberg A., 2000, *ApJ*, **542**, 235  
 Kirk J. G., Reville B., Huang Z.-Q., 2023, *MNRAS*, **519**, 1022  
 Lemoine M., Revenu B., 2006, *MNRAS*, **366**, 635  
 Lhaaso Collaboration et al., 2021, *Science*, **373**, 425  
 MAGIC Collaboration et al., 2019, *Nature*, **575**, 459  
 Matthews J. H., Bell A. R., Blundell K. M., 2020, *New Astron. Rev.*, **89**, 101543  
 Medvedev M. V., Zakutnyaya O. V., 2009, *ApJ*, **696**, 2269  
 Milosavljević M., Nakar E., 2006, *ApJ*, **651**, 979  
 Niemiec J., Ostrowski M., Pohl M., 2006, *ApJ*, **650**, 1020  
 Ostrowski M., 1993, *MNRAS*, **264**, 248  
 Plotnikov I., Grassi A., Grech M., 2018, *MNRAS*, **477**, 5238  
 Porth O., Buehler R., Olmi B., Komissarov S., Lamberts A., Amato E., Yuan Y., Rudy A., 2017, *Space Sci. Rev.*, **207**, 137  
 Press W. H., Teukolsky S. A., Vetterling W. T., Flannery B. P., 1992, Numerical recipes in FORTRAN. The art of scientific computing  
 Reville B., Bell A. R., 2014, *MNRAS*, **439**, 2050  
 Sironi L., Spitkovsky A., Arons J., 2013, *ApJ*, **771**, 54  
 Sironi L., Plotnikov I., Nättilä J., Beloborodov A. M., 2021, *Phys. Rev. Lett.*, **127**, 035101  
 Stockem A., Fiúza F., Fonseca R. A., Silva L. O., 2012, *ApJ*, **755**, 68  
 Summerlin E. J., Baring M. G., 2012, *ApJ*, **745**, 63  
 Takamoto M., Kirk J. G., 2015, *ApJ*, **809**, 29  
 Taylor A. M., Ahlers M., Hooper D., 2015, *Phys. Rev. D*, **92**, 063011  
 Thimmappa R., Stawarz Ł., Neilsen J., Ostrowski M., Reville B., 2022, *ApJ*, **941**, 204  
 Vanthieghem A., Lemoine M., Plotnikov I., Grassi A., Grech M., Gremillet L., Pelletier G., 2020, *Galaxies*, **8**, 33

## APPENDIX A: MONTE-CARLO CODE

In our Monte-Carlo implementation, we update individual trajectories over a time  $\Delta t$  using a 5th order Runge-Kutta integrator (Press et al. 1992) with an adaptive time step, and choose  $\Delta t$  such that the scattering is well resolved: Since the angular distribution function is concentrated in a cone of opening angle  $1/\Gamma_{\text{sh}}$  upstream, the condition we use there is  $\Delta t = 10^{-3}/(\Gamma_{\text{sh}}^2 \nu_+)$ . Downstream, on the other hand, the distribution function is expected to be a smoothly varying function of angle, so that  $\Delta t = 10^{-3}/\nu_-$ . After each step  $\Delta t$ , the direction of the momentum vector changed to account for small angle scattering, following the method described by Kirk & Schneider (1988). If a particle crosses the shock front during  $\Delta t$ , a root finding algorithm is applied to truncate this step such that it ends precisely on the shock surface. A Lorentz transformation is then made to the new frame and a new step is taken in this frame before applying the next scattering. Since we consider relativistic shocks, where the probability of a particle returning to the shock front after entering the downstream region is relatively low ( $\sim 50\%$ ) a particle splitting method is adopted. Each particle is initially assigned a weight of unity. On every third shock crossing from upstream to downstream, eight daughter particles are created, with a weight adjusted accordingly, and are then followed along statistically independent paths. We set an upper limit of ten on the number of generations of daughter particles.

At  $t = 0$ , particle trajectories are initiated isotropically immediately downstream of the shock with a Lorentz factor twice that of the shock. The energy spectrum, and angular distribution are found by recording the momentum  $\mathbf{p}$  each time a trajectory or one of its



daughters crosses the shock front, until either the time elapsed,  $t$  (measured in the downstream), reaches a pre-determined value, or the particle moves sufficiently far from the shock downstream. We find the results are insensitive to this boundary provided it exceeds either 10 times the gyro-radius  $\gamma c/\omega_-$  or 100 times the scattering mean free path  $c/\nu_d$ . In this way, a time-dependent solution of Eq. (1) is simulated with an injection term that is zero for  $t < 0$  and constant for  $t > 0$ .